RESEARCH

Polarization Insensitive Absorber with Wide Angular Stability Using Inclined Meander Line Resonators

Arumugam Sivanantham[1] · Inabathini Srinivasa Rao[1]

Abstract

A microwave absorber with an ultra-thin profile is created by drawing inspiration from wide-band metamaterials. This design incorporates a resistive layer and a convoluted meander line layer, separated by an air spacer. The convoluted meander lines are strategically placed along with resistors to enhance the absorption. The absorber is composed of two metallic-patterned layers. The initial metallic layer features a square ring with four resistors, the second metallic layer is a convoluted arrangement of inclined meander lines positioned at the four corners of the structure and coupled with square rings, and the bottom-most layer is coated with a conductive material. The distinct feature of the proposed structure lies in its exclusive co-polarized absorptivity, showcasing minimal cross-polarized absorption characteristics. The structure boasts a remarkable fractional bandwidth of 95%, maintaining an absorptivity exceeding 90% across the frequency range from 3.9 to 10.9 GHz. The structure's polarization-independent nature is thoroughly examined, revealing consistent absorption even when the polarization angle varies up to 90°. Angular stability analysis indicates that the absorber structure maintains stable absorption up to an incident angle of $45_\circ$. This proposed absorber holds promise as a viable option throughout the C-band and the lower section of the X-band for mitigating electromagnetic interference, making it well-suited for stealth applications.

Keywords Angular stability · Microwave absorber · Polarization insensitive · Resistive layer · Rozanov limit

Introduction

Frequency selective surface (FSS)-based structures are primary candidates in spatial filtering, absorbers, radar cross-section reductions, radomes, and stealth devices [1, 2]. Microwave absorbers that are designed with FSS have profound importance in stealth applications to absorb electromagnetic waves impinging on targets at arbitrary angles and in radar cross-section reduction [1]. During the Second World War, absorbers such as the Salisbury screen were designed using a quarter-wave transmission line-based impedance matching technique. But the absorber structures have a very narrow bandwidth. To increase the bandwidth, multiple layers of resistive sheets were placed at $\lambda/4$ distance from the ground layer in the Jaumann absorber. Despite the extended bandwidth, the structure has the drawback of large thickness [3, 4]. A perfect absorber with near-unity absorptivity was demonstrated in [5].

Unlike conventional microwave absorbers, metamaterial-inspired absorbers have attractive qualities like ultra-thin thickness, compact unit cell size, wider operating bandwidth, and stable absorption [6]. Single-layer design is preferred to achieve compactness in microwave, and mid-infrared frequencies [7]. The single-layer absorbers were designed with low profile size by reducing the thickness of the structure [8]. These structures were designed using single or double square loops, concentric circular rings [9, 10], scaled-in and scaled-up resonators of identical shapes, and cross-dipole resonators [11]. Fractal geometries and Minkowski loops [12] are used as metallic layers to achieve better absorption through ohmic loss and dielectric loss. But these absorber structures have a narrow bandwidth of absorption [13]. Hence, a multilayer structure is an ideal choice to attain a wide bandwidth of operation without increasing

Arumugam Sivanantham and Inabathini Srinivasa Rao contributed equally to this work.

✉ Inabathini Srinivasa Rao
   israo@vit.ac.in

   Arumugam Sivanantham
   sivanantham.a2018@vitstudent.ac.in

[1] School of Electronics Engineering, Vellore Institute of Technology, Vellore 632014, Tamil Nadu, India

the periodicity of the structure. Non-magnetic absorbers should fulfill the Rozanov thickness condition to attain wide bandwidth [14]. Reconfigurability can be imparted to attain multiband absorber structures using varactor diodes, [15] but the design complexity involves in maintaining bias potential. Meander line-based geometries and spiral structures can be used in designing wide-band absorption [16]. Resistive ink-based coatings are used as resonating layers to give a wide bandwidth. However, ensuring uniform thickness of the resistive ink is a challenging task [17]. Resistive sheet-based structures provide more loss and wide bandwidth [18, 19]. But the surface resistance of the sheets has fixed values. Hence, the usage of sheet-based absorbers is limited by available surface resistance. Wide-band absorption is achieved with multi-layered concentric rings with lumped resistors in [20]. Symmetric resonators can be used to create polarization-insensitive absorber structures [8, 21]. Broader bandwidths are often found in resistive element-based absorber systems [8, 22]. Multi-band absorption is achieved based on a dual-split square resonator in [23]. A cross-dipole-based split ring is used to achieve absorption of X-band frequencies in [24, 25]. Microstrip bend structure is used to achieve wide-band absorption in [26]. A lumped resistor-based loss mechanism is utilized to achieve wide-band absorption in [27]. Half-moon-shaped resonator with a multi-layer design is used to attain wide-band absorption in [28]. Dual split rings with H-shaped resonators are used in [29] to absorb C, X, and K band frequencies. Hence, multiple approaches such as circular split rings, square split rings, spiral loop with slot are adapted for the design of absorber structures with multi-band and wide-band absorption [7, 9, 20, 23–31]. However, the effect of cross-polarized reflection coefficient is not included in the evaluation of the absorptivity. Therefore, an absorber structure with pure co-polarized absorption and wide-band operation is an important design aspect to pursue. The design complexity can be reduced with less number of lumped resistors.

A wide-band microwave absorber is designed by arranging two metallic layers on inexpensive FR-4 substrates with dielectric permittivity (ϵ_r) of 4.4 and a loss tangent (tan δ) of 0.02. A stable absorption rate is attained by employing convoluted meander lines and resistive elements. By carefully arranging convoluted meander lines and resistive elements, a stable absorption rate can be achieved. The convoluted meander lines are strategically placed to create multiple reflections and scattering of the incident microwave signals, effectively increasing the path length and enhancing absorption. This design feature ensures that a wide range of frequencies can be absorbed efficiently, making the absorber suitable for various applications. In addition to the convoluted meander lines, resistive elements are incorporated into the design to further enhance absorption. These resistive elements dissipate the

energy of the incident microwaves as heat, thereby reducing reflection and transmission losses. The careful selection and placement of these resistive elements contribute to achieving a stable absorption rate across a wide frequency range.

Impedance matching is achieved by the air separation between the two metallic layers. Impedance matching is crucial in achieving optimal performance in microwave absorption systems. By ensuring that the impedance of the resistive elements matches that of the incident microwaves, maximum power transfer can be achieved. This impedance matching minimizes the reflection of microwaves back into the system, preventing energy loss and improving absorption efficiency. The bottom surface of the substrate on which the convoluted layer is patterned and coated with copper having conductivity $\sigma = 5.8 \times 10^7 \, Sm^{-1}$. The article is organized as follows. Unit cell geometrical design and construction is explained in the "Metamaterial Inspired Microwave Absorber (MIMAb) Structure and Design" section, methodology of analysis and performance comparison is given in the "Analysis of the Unit Cell and Discussion" section with a conclusion in the "Conclusion" section.

Metamaterial Inspired Microwave Absorber (MIMAb) Structure and Design

Absorber structures based on FSS should be designed with dielectric layers in between the resistive layer and the ground layer in order to selectively absorb the intended range of frequencies [1]. Absorptivity [4] is given by

$$A = 1 - \left|S_{11}\right|^2 - \left|S_{21}\right|^2 \tag{1}$$

where the reflected power is denoted by $\left|S_{11}\right|^2$ and the transmitted power is given by $\left|S_{21}\right|^2$. Absorption can be maximized by accomplishing two conditions simultaneously. The first condition is to have zero transmission, and the second condition is to have zero reflection. Transmission of electromagnetic energy through the structure is blocked by coating the bottom layer with metal that has a thickness greater than the skin depth [21]. Reflection is made zero by achieving an impedance matching mechanism. The input impedance of the structure is to be maintained to be equal to the free space impedance of 377 Ω. By keeping the reflection at zero level, peak absorption can be achieved. Maintaining the impedance matching between the structure and the free space for a wide range of frequencies is a challenging task. Since the absorption is inherently dependent on the resonance phenomenon, impedance mismatch occurs at frequencies other than the resonant frequency. Hence, to attain multiple absorption peaks, multiple resonances are to be created [15]. For the broad operation bandwidth of the absorber structure, a power dissipation mechanism based on lumped elements

can be imparted by incorporating resistors in the design [8]. Meander line-based structures provide a stronger inductive effect and larger magnetic induction.

The geometrical construction of the unit cell of the absorber structure is given in Fig. 1. The top resistive layer is constructed by a square ring of width $w_r = 0.5$ mm with four resistors for power dissipation as depicted in Fig. 1a. The bottom metallic-patterned layer is formed by convoluting three resonating structures. The outer layer is a square ring with corner slots. A circular ring is patterned with an outer radius of $r_o = 8$ mm, and an inner circular ring with a square slot is created to have a capacitive effect. The slot portion is patterned with convoluted meander lines with dimensions selected to avoid cross-talk between the resonators, as mentioned in Fig. 1b. The middle layer is an air spacer layer to achieve impedance matching as given in Fig. 1c. The side view of the unit cell is provided in Fig. 1d. The geometrical parameters of the unit cell are mentioned in Table 1.

Table 1 Unit cell parameters

Variable	Description	Value
p	Periodicity	17.0 mm
w_m	Meander line width	0.2 mm
r_o	Radius out	8.0 mm
r_1	Radius 2	7.4 mm
s_o	Slot 1	0.2 mm
s_1	Slot 2	9.7 mm
g_1	Gap 1	0.3 mm
g_2	Gap 2	0.2 mm
t_s	Substrate thickness	0.4 mm
R	Resistance	50.0 Ω
t_{air}	Air spacer height	7.8 mm
w_r	Resistive pattern width	0.5 mm
b	Resistive pattern period	12.0 mm

Analysis of the Unit Cell and Discussion

The full-wave electromagnetic simulation of the proposed absorber is carried out using ANSYS Electronic Desktop Environment 2020 (AEDT). The numerical computation tool is based on the finite element method. The full-wave simulation of the absorber structure requires the simulation of a large finite array. But the simulation of the finite array is computationally intensive. Hence, an efficient method is to construct a unit cell of the array and to apply periodic boundary conditions along X and Y directions.

Fig. 1 Unit cell geometry. **a** Resistive layer, **b** convoluted layer, **c** isometric view, **d** side view
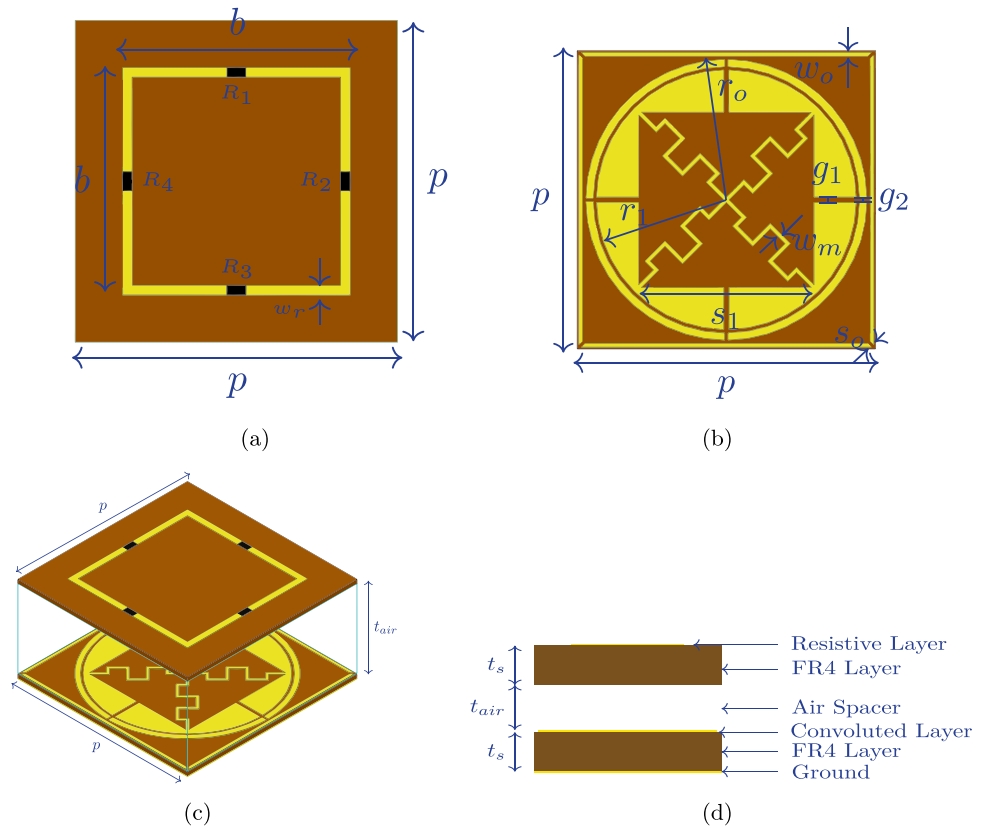
The periodic boundary conditions is realized through the application of the primary and the secondary boundaries. As a result of the periodic boundary conditions, the electric field distribution is uniform throughout the periodic structure. Automatic adaptive meshing is performed in the Ansys AEDT. The excitation to the unit cell is applied by placing the Floquet port on the top surface of the unit cell along the $+ Z$ axis. The Floquet port represents a plane wave with its characteristics dependent on the geometry of the unit cell. The excitation port is positioned at a distance of $\lambda/4$ from the surface of the unit cell to reduce the effect of high-frequency degenerate modes. To investigate the behavior of the unit cell in each operating frequency, a discrete type of analysis is preferred in the simulation. In order to increase the speed of computation, the high-performance computing (HPC) option is utilized in the Ansys AEDT tool. By using the HPC option, the parametric sweep is performed with less computation time using distributed analysis in multiple machines [2].

Reflectivity Under Normal Incidence

The reflection and the absorption characteristics of the absorber structure are analyzed as shown in Fig. 2. The value of reflectivity is less than -10 dB for the frequency range 3.9 GHz to 10.9 GHz as observed in Fig. 2a. The fact that the reflectivity is significantly low within this frequency range indicates that a large portion of the incident electromagnetic energy is being absorbed rather than reflected. It is evident that the absorption bandwidth is extending from 3.9 GHz to 10.9 GHz, covering a wide frequency band. The achievement of wide-band absorption in this scenario can be attributed to the presence of resistive elements within the system. The lumped resistors play a prominent role in dissipating electrical energy as heat, preventing any reflection or transmission of the energy. With the high electrical resistance, the lumped resistors efficiently convert electrical energy into thermal energy, ensuring that the absorbed frequencies are effectively absorbed and not reflected back into the system.

Absorption and Polarization Conversion Ratio Characteristics

Absorption characteristics are compared along with the polarization conversion ratio in order to ensure pure co-polarized absorption behavior. The co-polarized reflection coefficient [4] is given by $r_{yy} = \left| E_{yr}/E_i \right|$ and the cross-polarized reflection coefficient [4] is given by $r_{xy} = \left| E_{xr}/E_i \right|$, where E_{yr} is the y-polarized reflected wave, E_{xr} is the x-polarized reflected wave, and E_i is the y-polarized incident wave. polarization conversion ratio (PCR) [4] is given by

$$PCR = \frac{r_{xy}^2}{r_{xy}^2 + r_{yy}^2} \tag{2}$$

The designed structure has cross-polarized absorption less than 0.1% and the absorption is purely co-polarized absorption as noticed in Fig. 2b.

Parametric Variation

Parametric analysis is carried out to achieve the optimized design of the microwave absorber. By systematically varying the geometric variables of the unit cell, one can determine the values that result in the better absorption characteristics. The geometrical values of the unit cell play a significant role in determining the overall performance of the microwave absorber. These values include parameters such as the size, shape, arrangement, and the dimensions of the resonating elements and dielectric property, within the unit cell. Each of these variables can have a direct impact on the absorption
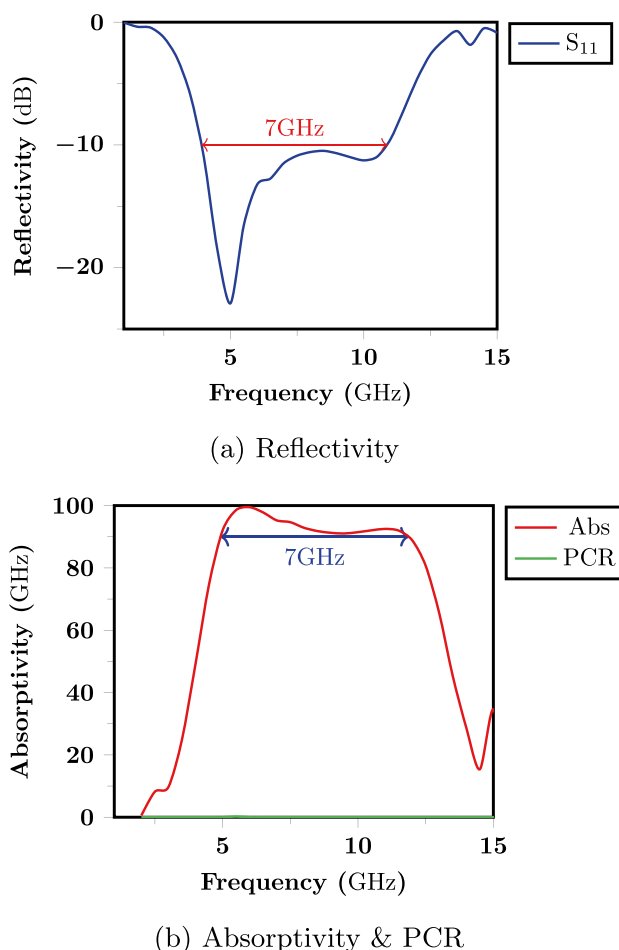

(a) Reflectivity

(b) Absorptivity & PCR

Fig. 2 Simulated reflection, absorption and polarization conversion ratio (PCR) characteristics

(a) Impact of substrate thickness

(b) Impact of airspacer height

(c) Impact of lumped resistor
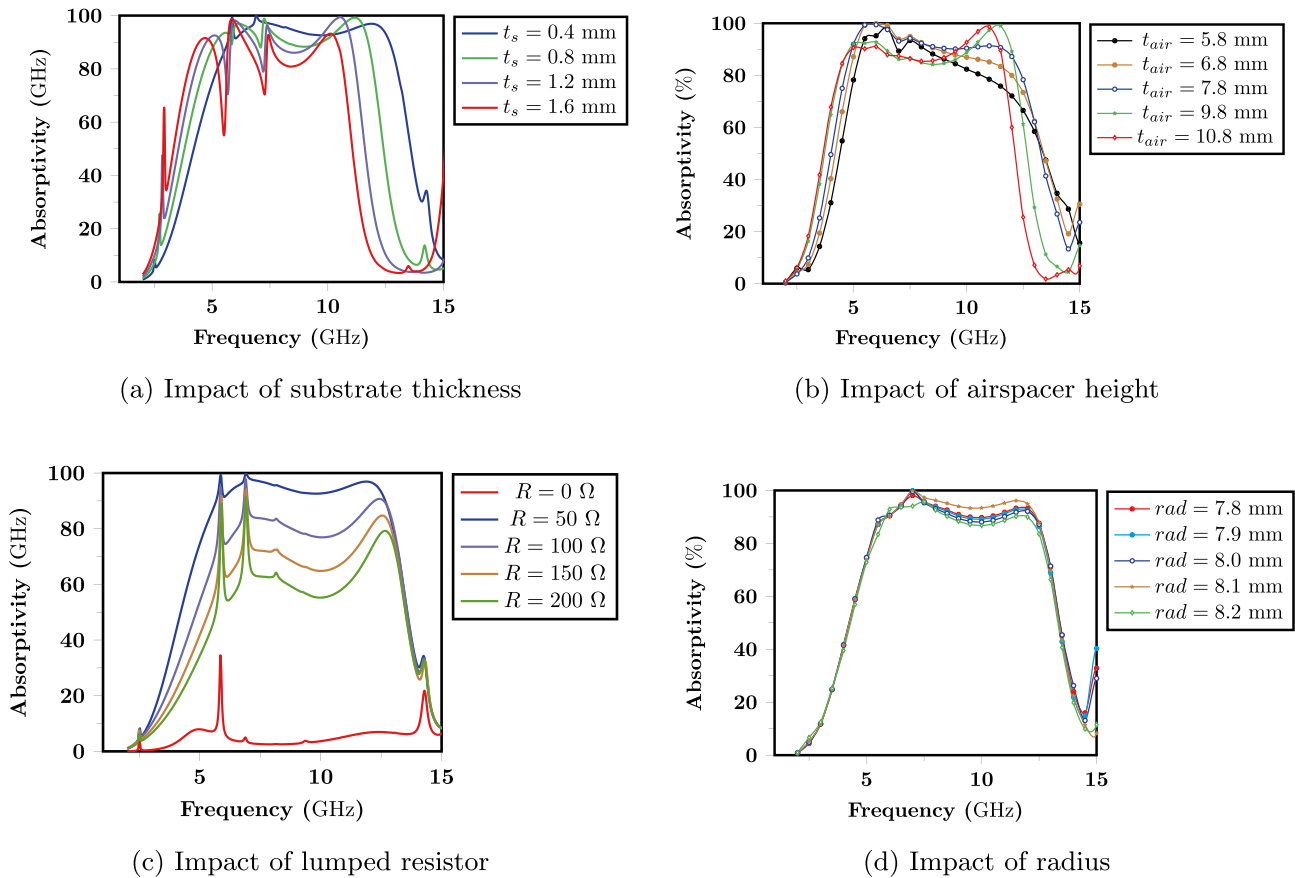

(d) Impact of radius

Fig. 3 Simulated absorption characteristics with geometric parameters variation

characteristics and the bandwidth of the absorber. Through parametric analysis, we can investigate a wide range of geometric configurations and evaluate their impact on absorption characteristics as depicted in Fig. 3. This involves systematically varying one or more geometric variables while keeping other parameters constant. By doing so, we can observe how changes in these variables affect key performance metrics such as reflection loss, absorption bandwidth, and impedance matching. Parametric variation for each variable is accelerated with the HPC option in AEDT using distributed analysis.

Effect of Substrate Thickness

Absorption bandwidth is influenced by the impedance matching between the free space impedance and the impedance of the absorber structure. The impedance of the dielectric layer 1 with metallic bottom layer is dependent on the thickness of the substrate [8] as given in

$$Z_{sub1} = j\frac{Z_0}{\sqrt{\epsilon_r}} \tan(\beta_2 t_s) \tag{3}$$

where $\frac{Z_0}{\sqrt{\epsilon_r}}$ is the characteristic impedance, $\beta_2 = \frac{2\pi\sqrt{\epsilon_r}}{\lambda}$ is the phase constant of the substrate layer 1, and t_s is the thickness of the substrate. Similarly, the impedance of the substrate layer 2 is given by

$$Z_{sub2} = \frac{Z_0}{\sqrt{\epsilon_r}} \left[\frac{Z_{air} + j\frac{Z_0}{\sqrt{\epsilon_r}} \tan(\beta_2 t_s)}{\frac{Z_0}{\sqrt{\epsilon_r}} + jZ_{air} \tan(\beta_2 t_s)} \right] \tag{4}$$

where $\frac{Z_0}{\sqrt{\epsilon_r}}$ is the characteristic impedance, $\beta_2 = \frac{2\pi\sqrt{\epsilon_r}}{\lambda}$ is the phase constant of the substrate layer 2. The impedance matching is influenced by substrate thickness (t_s) of both FR-4 dielectric layers and the thickness is varied from 0.4 mm to 1.6 mm to determine the impact on absorption rate. The quality factor of the structure decreases when the substrate thickness is at $t_s = 0.4$ mm. Hence, the wide absorption bandwidth with absorptivity greater than 90% is obtained at $t_s = 0.4$ mm, as observed in Fig. 3a. A reduction in the substrate thickness leads to a better absorption rate.

Effect of Air Spacer Height

Impedance of the air spacer layer is given by

$$Z_{air} = Z_0 \left[\frac{Z_2 + jZ_0 \tan(\beta_1 t_{air})}{Z_0 + jZ_2 \tan(\beta_1 t_{air})} \right] \quad (5)$$

Air spacer height (t_{air}) is significant for extending bandwidth by reducing the lower resonant frequency of the structure. Hence, it is varied from 5.8 mm to 10.8 mm to determine the impact on absorptivity. In tune with increasing air spacer thickness, the effective impedance of the structure changes, and hence the absorption rate is greater than 90% when t_{air} = 7.8 mm as observed in Fig. 3b.

Effect of Resistance Variation

Resistance (R) is varied from 0 Ω to 200 Ω to determine the impact on absorption rate. Absorption is close to zero when there is no resistance. Absorption is more than 90 % when the resistance is at 50 Ω. Increasing the resistance value beyond 50 Ω, leads to a reduction in absorption for resistance values of 100 Ω, 150 Ω, and 200 Ω as observed in Fig. 3c. The quality factor of the structure is reduced with the introduction of the resistors and hence the bandwidth is increased. The loss in the unit cell is predominantly due to ohmic loss from the lumped resistors.

Effect of Radius Variation

To assess the effect on absorption rate, the radius (r_o) is varied from 7.8 mm to 8.2 mm. In tune with the increasing radius, the reactive inductance of the resonator increases. Consequently, the impedance of the structure varies as the radius changes, which lowers the absorption frequency. When the radius is 8 mm, stable absorptivity with an absorption rate of more than 90% is noted, as shown in Fig. 3d.

Significance of Dielectric Permittivity ϵ_r on the Absorption

The dielectric permittivity of the substrate (ϵ_r) is the crucial factor in controlling the resonant frequency of the absorber structure. Substrates with small ϵ_r values have higher resonant frequency as mentioned in Fig. 4. Left shift is observed (resonant frequency gets reduced) when a dielectric substrate of higher ϵ_r is used. Consequently, low-frequency resonance is reduced. Due to this the bandwidth gets widened when the FR-4 substrate with ϵ_r = 4.4, tan δ = 0.02 is used. Better absorption is noted for FR4 substrate than other substrates in lower resonant frequencies.

Stagewise Implementation of the Absorber Structure

In order to induce multiple resonances or to attain wide-band absorption, multiple resonating structures are to be patterned
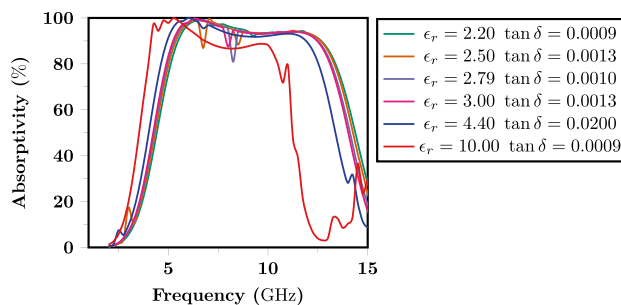

Fig. 4 Comparison of simulated absorptivity across substrates with different relative permittivity (ϵ_r)

on the grounded substrate. The number of resonating structures is also limited by the periodicity of the unit cell. Because, if the periodicity of the unit cell is increased, grating lobes will appear. This will lead to poor angular stability of the structure. Hence, the optimum number of resonators is placed on the FSS layer on the bottom substrate. Nevertheless, the absorption is around 25% when the FSS layer is analyzed. The FSS layer along with the meander line geometry has absorption close to 40%. The absorption bandwidth can be widened by combining the two layers. The resistive layer in the form of a square ring with four lumped resistors embedded in the arms of the ring is investigated. The resistive layer shows very less absorption without any air spacer layer. As observed in Fig. 5, the absorption is prominent with absorption more than 90% in the frequency range from 3.9 to 10.9 GHz when the resistive layer is placed on the FSS layer with an air spacer layer between the two layers.

Normal Incidence-Effect of Polarization Angle Variation

The polarization-independent behavior of the structure is analyzed as shown in Fig. 6. By varying the polarization angle from 0° to 90°, we can observe how the absorber structure performs under different orientations of the incident electric
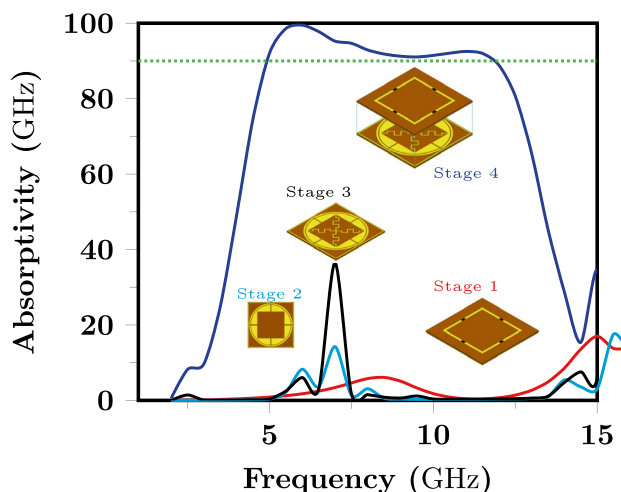

Fig. 5 Absorption characteristics for each layer of the structure
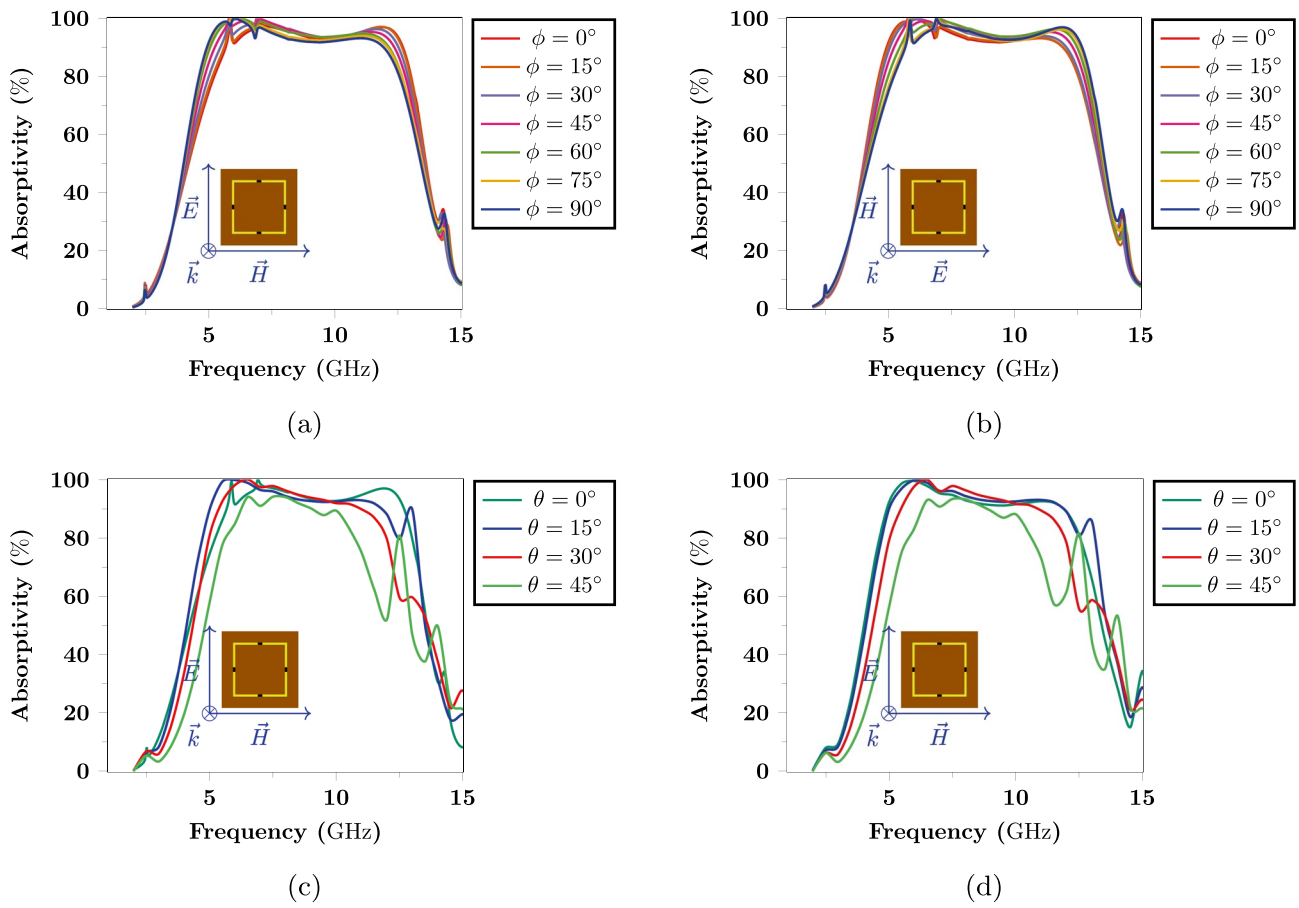
Fig. 6 Simulated absorption characteristics. **a** Effect of polarization angle variation under TE mode, **b** effect of polarization angle variation under TM mode, **c** effect of incident angle variation under TE mode, **d** effect of incident angle variation under TM mode

field. At a polarization angle of 0°, the electric field vector is aligned with the symmetric axis of the absorber, resulting in the maximum absorptivity. As we gradually rotate the polarization angle towards 90°, where the electric field vector becomes perpendicular to the symmetry axis, we may expect a decrease in absorption efficiency. However, due to the circular symmetry of the absorber structure, it remains insensitive to these changes in polarization angle. This means that regardless of whether the electric field vector is aligned with or perpendicular to its symmetry axis, the absorber will maintain its high absorption efficiency. Absorptivity is found to be stable with more than 90% absorption rate for the entire polarization angle variation. Hence, the stability of the absorber structure for both the transverse electric (TE) and the transverse magnetic (TM) polarization is confirmed as observed in Fig. 6a and b.

Oblique Incidence-Effect of Incident Angle Variation

Analyzing the behavior of the structure for oblique incident angles is crucial because, in real-world scenarios, the electromagnetic waves impinge on the targets at arbitrary incident angles [1]. The interaction between the electromagnetic waves and the material is highly dependent on the angle of incidence. When the em waves strike the surface at an oblique angle, their energy distribution changes, resulting in the variations in reflection, transmission, and absorption characteristics. Therefore, studying the response of the absorbers to oblique incident angles helps in understanding their effectiveness and performance [32]. Absorption is found to be more than 90% for the incident angle from $\theta = 0°$ to $\theta = 45°$ beyond which the absorption reduces drastically [1] as observed in Fig. 6c and d.

Parameter Extraction

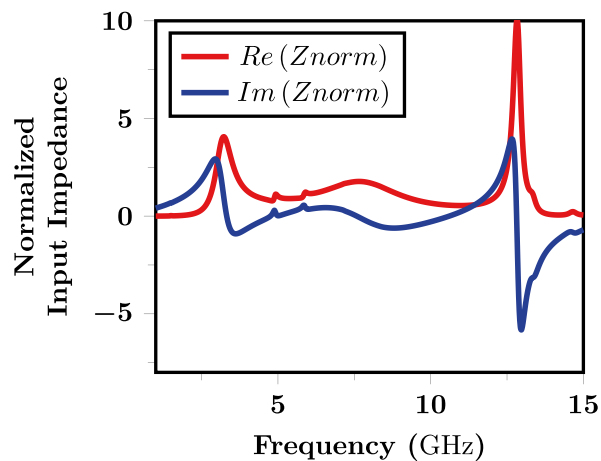### Effective Permeability

The effective permeability (μ_{eff}) is given by [4]

$$\mu_{\text{eff}} = 1 + \frac{2j}{k_0 h}\left(\frac{1 + S_{11}}{1 - S_{11}}\right) \tag{6}$$
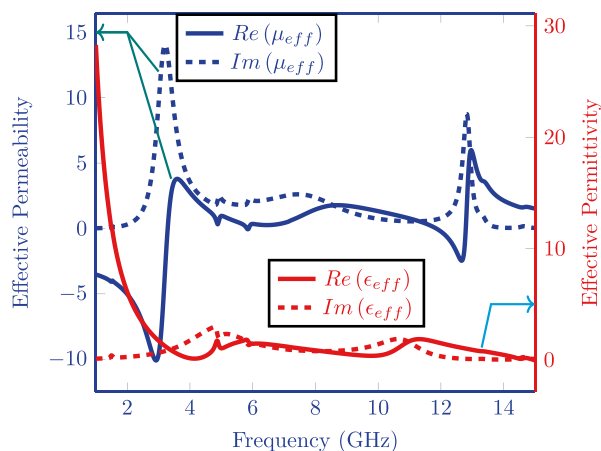
(a) Effective permeability (μ_{eff}) & Effective permittivity (ϵ_{eff})
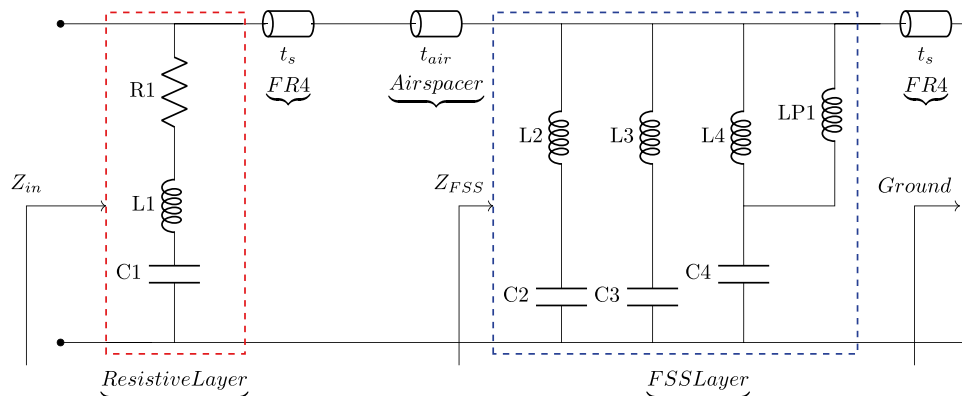

(b) Normalized input impedance

Fig. 7 Simulated parameter extraction characteristics

where $k_0 = \left(\frac{2\pi}{\lambda}\right)$ is the wavenumber of the free space, S_{11} is the reflection coefficient under normal incidence and h is the sum of thickness of substrate layers with air spacer

height. Unit cell thickness is given by $h = t_s + t_{air} + t_s = 8.6$ mm. The real part of the effective permeability is found to be varying as a function of frequency, proving the controlling ability of the electromagnetic properties of the absorber structure. The imaginary term has larger magnitudes as the term is responsible for loss and hence confirms the metamaterial behavior of the structure as observed in Fig. 7a.

Effective Permittivity

The effective permittivity (ϵ_{eff}) is given by [33]

$$\epsilon_{eff} = 1 + \frac{2j}{k_0 h}\left(\frac{1 - S_{11}}{1 + S_{11}}\right) \qquad (7)$$

The real part and imaginary part of the effective permittivity have a contrary sign to one another. The imaginary term has larger magnitudes as the term is responsible for loss and hence confirms the metamaterial behavior of the structure as observed in Fig. 7a.

Significance of the Extracted Parameters

The proposed absorber structure can be analyzed with the help of the effective medium theory of metamaterial structures. The effective permittivity is a complex function of frequency denoted as $\epsilon_{eff} = \epsilon'(\omega) + j\epsilon''(\omega)$ and the effective permeability is denoted as $\mu_{eff} = \mu'(\omega) + j\mu''(\omega)$. The absorber structure attains maximum absorption in the frequency ranges where the complex quantities of effective permeability and the effective permittivity are almost equal in the operating frequency range as depicted in Fig. 7. Hence, the effective medium parameters are modified by means of optimized dimensions in the absorber structure to attain good absorption.

Normalized Input Impedance

Based on the principle of effective medium theory, the effective impedance of the absorber structure should be

Fig. 8 Equivalent circuit model of the absorber structure
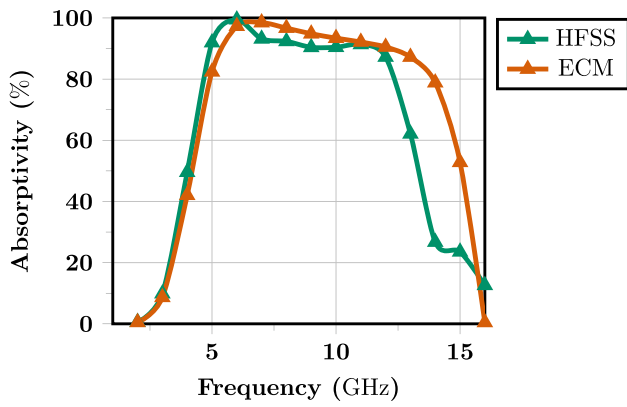
Fig. 9 Comparison of circuit simulated response using AWR with full-wave simulated response using HFSS

equal to the free space impedance value 377 Ω. The effective impedance of the structure is dependent on electric permittivity $\epsilon(\omega)$ and the magnetic permeability $\mu(\omega)$. The

effective impedance can be determined from the extracted parameters of the absorber structure.

The normalized input impedance (Z_{norm}) is given by [8, 23]

$$Z_{norm} = \sqrt{\frac{\mu_{eff}(\omega)}{\epsilon_{eff}(\omega)}} = \sqrt{\frac{1 + S_{11}^2(\omega) - S_{21}^2(\omega)}{1 - S_{11}^2(\omega) - S_{21}^2(\omega)}} \tag{8}$$

Since the transmitted power is made zero by means of the metallic ground layer, the normalized input impedance is simplified as

$$Z_{norm} = \frac{1 + S_{11}}{1 - S_{11}} \tag{9}$$

The real part of normalized input impedance remains unity throughout the range of operating frequency and the imaginary part stays at zero. Hence, the impedance of the structure is maintained to be equal to that of free space impedance for
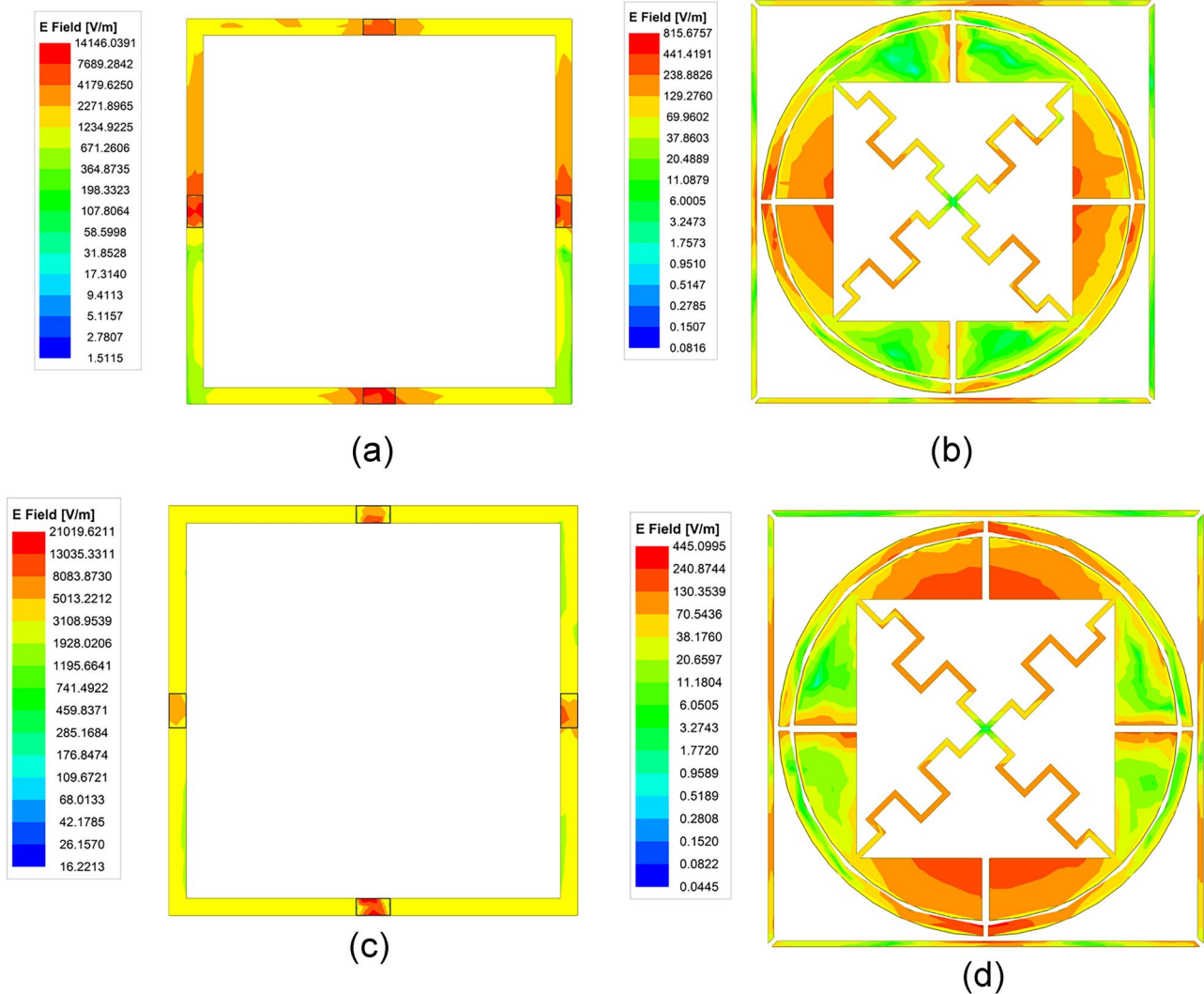

(a)

(b)

(c)

(d)

Fig. 10 Simulated E-field distribution. **a** Resistive layer at 6 GHz -TE, **b** FSS layer at 10 GHz -TE, **c** resistive layer at 6 GHz -TM, **d** FSS layer at 10 GHz -TM

the entire operating frequency range thereby achieving wide absorption as observed in Fig. 7b. By comparing this model with other existing absorber structures, we can gain valuable insights into the underlying physics and optimize the design for enhanced performance.

Equivalent Circuit Model

The equivalent circuit model of the proposed absorber structure, as shown in Fig. 8, provides a comprehensive understanding of the absorption mechanism. The equivalent circuit model consists of various components that represent different aspects of the absorber structure. These components include resistors, capacitors, and inductors, each corresponding to specific physical phenomena occurring within the structure.

Analyzing this model allows us to identify the dominant mechanisms responsible for absorption. A significant resistance component in the circuit indicates that dissipation plays a crucial role in absorbing incident energy. On the other hand, if we notice a substantial capacitance or inductance component, it suggests that reactive elements are contributing significantly to absorption. By quantifying these components and their interplay within the equivalent circuit model, we can determine how effectively our proposed absorber structure absorbs electromagnetic waves across different frequencies. The top resistive layer is denoted as a series RLC circuit. FR-4 substrate at the top layer is modeled as a transmission line with characteristic impedance as $\frac{Z_0}{\epsilon_r}$ and thickness as t_s. The air spacer is modeled as a transmission line with characteristic impedance as Z_0 and thickness as t_{air}. Metallic patterns on
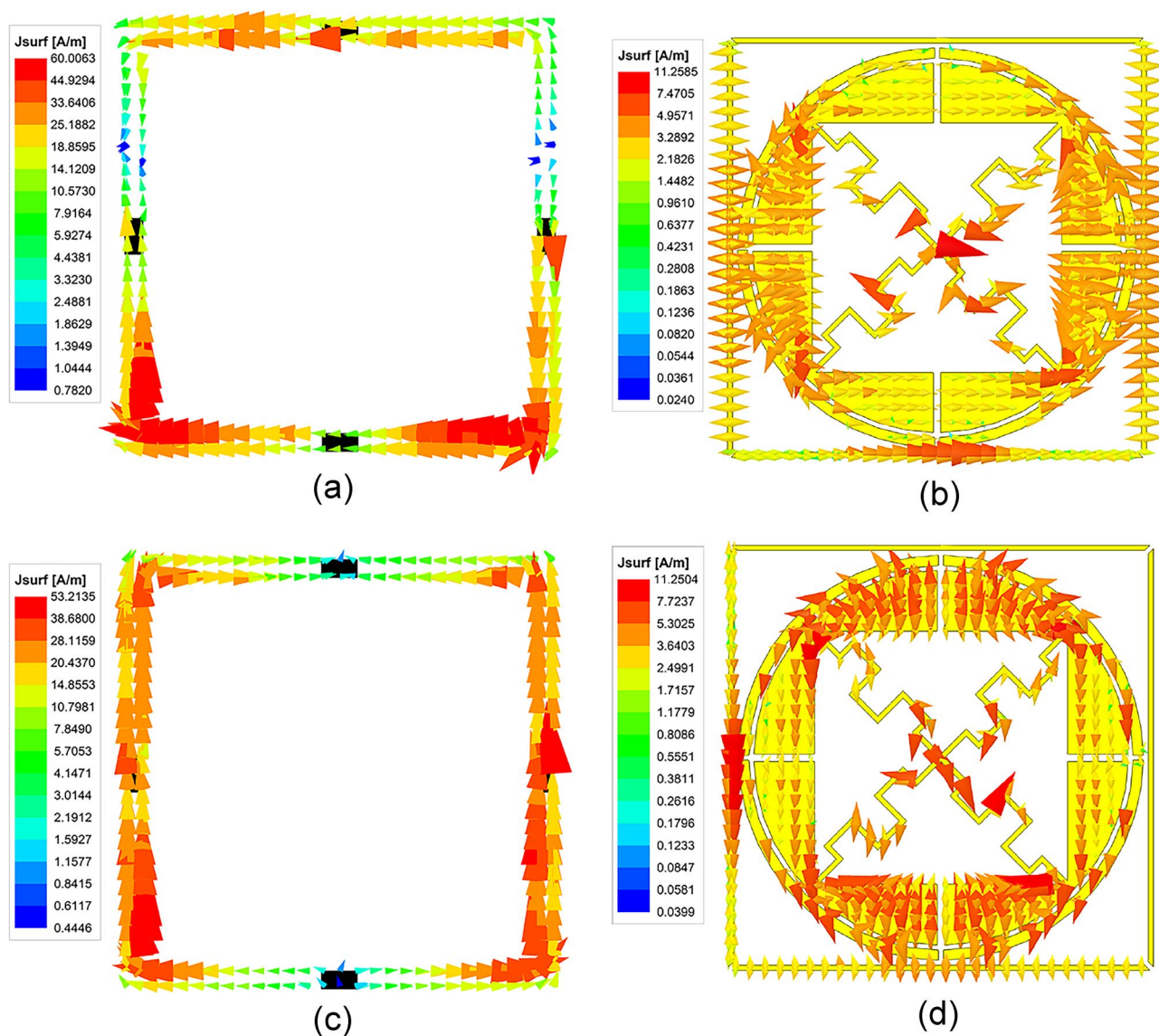

Fig. 11 Simulated surface current distribution. **a** Resistive layer at 6 GHz -TE, **b** FSS layer at 10 GHz -TE, **c** resistive layer at 6 GHz -TM, **d** FSS layer at 10 GHz -TM
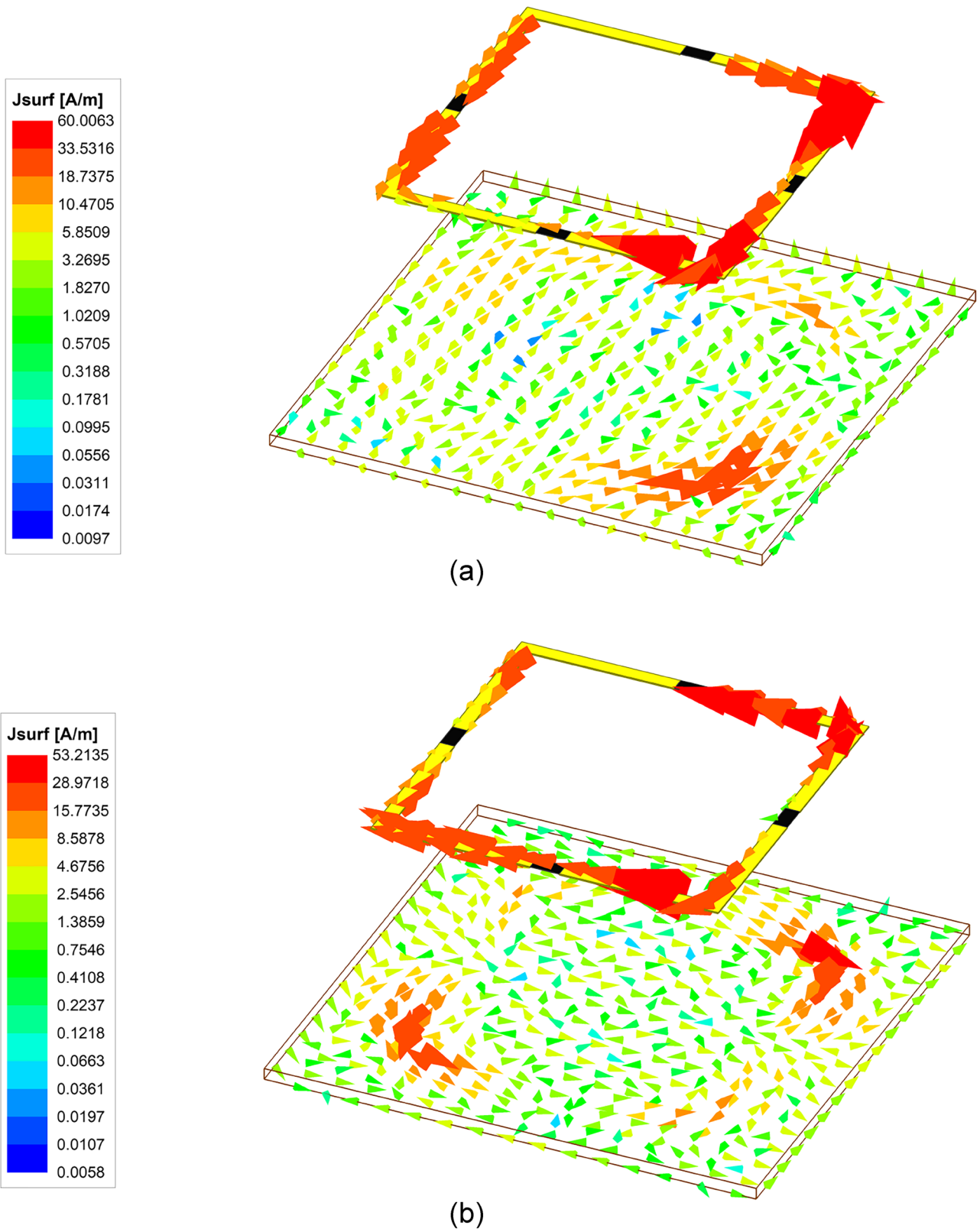
Fig. 12 Simulated surface current distribution on the bottom layer. **a** TE polarization, **b** TM polarization

bottom FSS layers are modeled by the parallel combination of series LC circuits. The grounded substrate at the bottom layer is modeled as a short-circuited transmission line with characteristic impedance $\frac{Z_0}{\epsilon_r}$ and thickness as t_s. Peak absorption is obtained in the frequency range when the reactance cancellation between the layers occurs. The absorption is maximum when the input impedance of the structure matches the impedance of free space.

Absorption response of the equivalent circuit using Applied Wave Research (AWR) circuit simulation tool and Ansys AEDT full-wave simulation tool are having good contract as observed in Fig. 9.

Field Distribution

Electric Field Distribution

The electric field distribution is analyzed on the surface of the absorber structure, to understand the electric resonance as depicted in Fig. 10. A well-designed absorber should exhibit a high electric field strength in regions where absorption is desired, indicating efficient energy conversion from electromagnetic waves to heat.

Furthermore, analyzing the electric field plot can help identify any unwanted reflections or standing waves within the absorber structure. These reflections can lead to poor absorption performance or even damage to sensitive components nearby. By studying the electric field distribution, the design can be optimized to improve absorptivity. The top resistive layer has prominent E-field distribution in the entire band of operating frequencies with peak magnitude at 6 GHz. The bottom convoluted meander line layer has E-field distribution through the meander line structures during TM polarization for the frequency range of 7 GHz. E-field distribution confirms the formation of electric resonance on the absorber structure as observed in Fig. 10a–d.

Surface Current Distribution

The surface current distribution illustrates the flow of electrical current within the absorber structure. It provides insight about the direction of current on the surface of the structure. by highlighting regions where energy dissipation occurs due to ohmic loss. Surface current distribution is analyzed to identify the formation of magnetic resonance in the absorber structure as given in Figs. 11 and 12. Peak magnitude is noticed on the resistance region hence confirming the absorption due to resistors in the form of heat. In addition to that, the corners along the meander line structures on the FSS layer also have larger magnitudes of surface current distribution as observed in Fig. 11a–d. The direction of the surface current density vector is found to be anti-parallel in
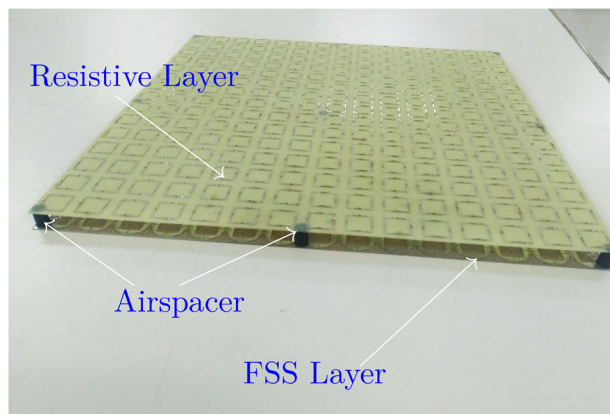
(a) Fabricated absorber prototype
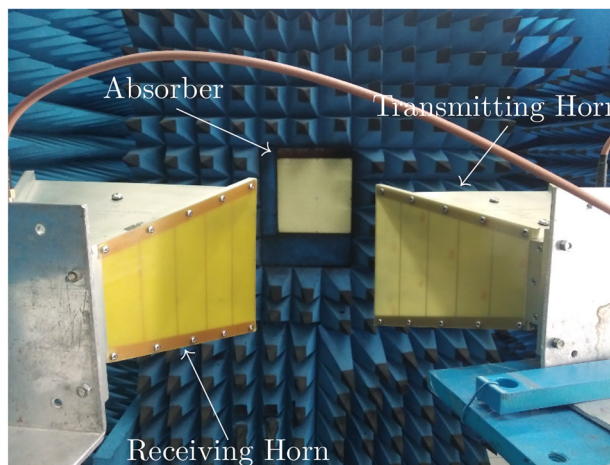
(b) Absorber structure in anechoic chamber

Fig. 13 Absorber measurement setup

the bottom ground layer to that of the top resistive layer. This behavior confirms the induction of magnetic resonance as observed in Fig. 12a and b.

Experimental Validation of the Absorption

The absorber structure is fabricated using the printed circuit board (PCB) technique with an array size of 15×15 unit cells of size 255 mm × 255 mm on FR-4 substrate as shown in Fig. 13a. Measurements of reflectivity, absorptivity, polarization angle dependency, and incident angle stability are carried out in an anechoic chamber. Two horn antennas one of which acts as a transmitting antenna and the other acting as a receiving antenna, are used to perform the characterization of the absorber structure. Horn antennas are placed at a distance of 1.5 m from the absorber sample to fulfill far-field measurement conditions as given in Fig. 13b. The effect of noise that is present in the anechoic chamber is cancelled out during measurement as follows: Initially, the reflectivity
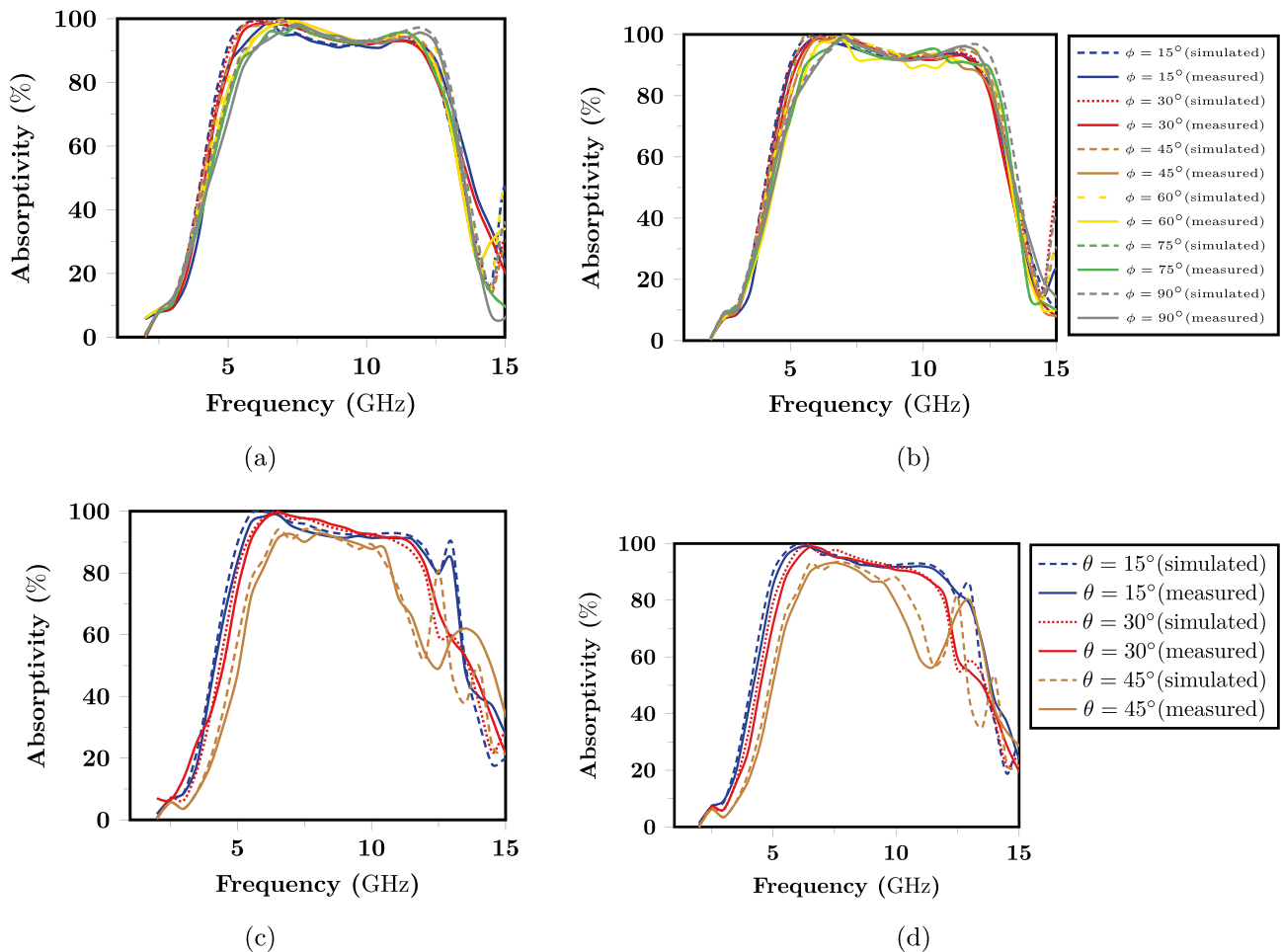
Fig. 14 Comparison of measured absorption with simulated behavior. **a** Effect of polarization angle variation under TE mode, **b** effect of polarization angle variation under TM mode, **c** effect of incident angle variation under TE mode, **d** effect of incident angle variation under TM mode

of a copper plate with an identical dimension to that of the designed absorber structure is measured.

Then the proposed MIMAB structure is placed in the sample holder of the anechoic chamber to measure its reflectivity. With this, the reflectivity under normal incidence is obtained. The difference between the two reflectivity values gives the actual reflection from the absorber structure. The Vector Network Analyzer N9951A records the reflection behavior of the fabricated array of unit cells.

The polarization angle is varied, and the absorption is found to be stable for a wide range of frequencies under normal incidence conditions as depicted in Fig. 14a and b. The angular stability of the absorber structure is measured by placing the two horn antennas in an inclined position to analyze the oblique incidence behavior. A pyramidal absorber is placed between the transmitting and receiving antennas to block direct talk during the measurement. The incident angle is varied in steps of 15° from 0° to 60° and

the absorption of the structure is found to be stable with absorptivity greater than 90% upto 45° as given in Fig. 14c and d. Validation of the simulated absorptivity is performed by comparing the simulated results with the measured values as observed in Fig. 14. The minimal deviation of the measured absorption from the simulated behavior is due to the scattering from the lumped elements, the finite size of the absorber prototype, and edge diffraction arising out of it. The theoretical minimum Rozanov thickness [14] for a non-magnetic absorber structure at the lowest operating frequency of 3.9 GHz is $d_{theory} = 5.8$ mm, while the actual thickness proposed structure is $d_{real} = 8.6$ mm. The performance indicator of the absorber structure is given by $C = \frac{d_{theory}}{d_{real}}\% = 67\%$ shows the resemblance of the proposed absorber with the ideal non-magnetic absorber. Performance comparison is given in Table 2. The proposed structure has a better absorption bandwidth with a minimal number of four resistors.

Table 2 Performance comparison with reported absorber structures

Reference	Frequency range (GHz)	Fractional bandwidth (%)	Periodicity (λ_L)	Relative thickness (λ_L)	Predominant loss element	Polarization purity
[9]	8.00−13.00	51.16	0.414	0.082	Dielectric	Cross polarized
[10]	6.70−20.58	101.70	0.28	0.067	8 Resistors	Co-polarized
[11]	5.30−11.20	70.02	0.243	0.08	4 Resistors	Co-polarized
[22]	8.20−13.40	48.10	0.419	0.082	8 Resistors	Cross polarized
[24]	8.50−16.00	61.00	0.0353	0.056	Dielectric	Cross polarized
[31]	11.40−20.00	54.45	0.139	0.061	Dielectric	Cross polarized
[34]	5.10−14.07	93.58	DNP	0.112	Resistive sheet	Co-polarized
[35]	10.45−17.64	51.19	0.194	0.054	Dielectric	Cross polarized
[36]	8.00−18.00	76.92	0.133	0.077	Dielectric	Cross polarized
Proposed MIMAB	3.90−10.90	95.00	0.22	0.111	4 Resistors	Co-polarized

Conclusion

In conclusion, the development of an ultra-thin metamaterial absorber designed for wide-band absorption achieves notable results, showcasing an impressive 7 GHz bandwidth with absorption surpassing 90%, and the total thickness of the structure is $0.117\lambda_L$, where λ_L is the wavelength at the lowest operating frequency. The absorber's exceptional performance is attributed to the strategic arrangement of resonating elements within the unit cell, resulting in remarkable polarization-insensitive behavior. This feature is derived from the symmetric configuration of the metallic-patterned layers. Demonstrating angular stability up to an incident angle of 45°, the structure exhibits minimal cross-polarized absorption, emphasizing its pure co-polarized absorption characteristics. In essence, the developed absorber stands as a noteworthy contribution to the field, showcasing advanced features that make it a promising solution for a range of practical applications. including minimizing interference and enhancing capabilities in stealth applications.

Data Availability Not applicable.

Code Availability Not applicable.

Declarations

Ethics Approval Not applicable.

Consent to Participate Not applicable.

Consent for Publication Not applicable.

Competing Interests The authors declare no competing interests.

References

1. Munk BA (2005) Frequency selective surfaces: theory and design. John Wiley & Sons
2. Vinoy KJ, Jha RM (1995) Trends in radar absorbing materials technology. Sadhana 20:815–850
3. Ghosh S, Bhattacharyya S, Srivastava KV (2016) Design, characterisation and fabrication of a broadband polarisation-insensitive multi-layer circuit analogue absorber. IET Microwaves Antennas Propag 10(8):850–855
4. Kalraiya S, Chaudhary RK, Gangwar RK (2021) Polarization independent triple band ultrathin conformal metamaterial absorber for C-and X-frequency bands. AEU Int J Electron Commun 135:153752
5. Landy NI, Sajuyigbe S, Mock JJ, Smith DR, Padilla WJ (2008) Perfect metamaterial absorber. Phys Rev Lett 100(20):207402
6. Bhattacharyya S, Ghosh S, Chaurasiya D, Srivastava KV (2015) Wide-angle broadband microwave metamaterial absorber with octave bandwidth. IET Microwaves Antennas Propag 9:1160–1166. ISSN 17518733. https://doi.org/10.1049/iet-map.2014.0632
7. Singhal S (2022) Wide incident angle insensitive ultrawideband mid-infrared perfect absorber. Optik 249:168295
8. Kalraiya S, Chaudhary RK, Abdalla MA (2022) Resistor loaded wideband conformal metamaterial absorber for curved surfaces application. AEU - Int J Electron Commun 143:154033
9. Ghosh S, Bhattacharyya S, Chaurasiya D, Srivastava KV (2015) An ultrawideband ultrathin metamaterial absorber based on circular split rings. IEEE Antennas Wirel Propag Lett 14:1172–1175
10. Sambhav S, Ghosh J, Singh AK (2021) Ultra-wideband polarization insensitive thin absorber based on resistive concentric circular rings. IEEE Trans Electromagn Compat 63(5):1333–1340
11. Kundu D, Mohan A, Chakrabarty A (2016) Single-layer wideband microwave absorber using array of crossed dipoles. IEEE Antennas Wirel Propag Lett 15:1589–1592
12. Zhang X, Wu W, Huang L, Ma Y, Yuan N (2019) Design of dual-absorptive-bands frequency selective rasorber with minkowski loop arrays. IEEE Antennas Wirel Propag Lett 18(9):1843–1847

13. Ghosh A, Banerjee A, Das S (2019) Design of compact polarization insensitive triple bandstop frequency selective surface with high stability under oblique incidence. Radioengineering 28:552–558 ISSN 12102512. https://doi.org/10.13164/re.2019.0552

14. Rozanov KN (2000) Ultimate thickness to bandwidth ratio of radar absorbers. IEEE Trans Antennas Propag 48(8):1230–1234

15. Ghosh S, Srivastava KV (2020) A dual-band tunable frequency selective surface with independent wideband tuning. IEEE Antennas Wirel Propag Lett 19(10):1808–1812

16. Coomar S, Mondal S, Sanyal R (2022) Polarization-insensitive ultrathin fractal shaped frequency selective surface for ultra wide band shielding. AEU Int J Electron Commun 147. ISSN 16180399. https://doi.org/10.1016/j.aeue.2022.154141

17. Dhumal A, Bisht MS, Bhardwaj A, Saikia M, Malik S, Srivastava K V(2022) Screen printed polarization independent microwave absorber for wideband rcs reduction. IEEE Trans Electromagn Compat

18. Kumar A, Reddy GS, Jyotibhusan P (2022) Highly angular-stable optically transparent microwave absorber with wide absorption bandwidth. IEEE Letters on Electromagnetic Compatibility Practice and Applications 4(4):114–119

19. Li Y, Sun Z, Li E-P (2023) Design and analysis of a miniaturized broadband resistive film absorber to reduce chip system radiation. IEEE Trans Electromagn Compat

20. Inbavalli VP, Sakthivel VP, Venkatesh C, TR SK (2023) Design of broadband circuit analog absorber with optimal thickness for stable angular response in C, X, Ku, and K bands. IEEE Trans Electromagn Compat

21. Ramya S, Rao IS (2018) An ultra-thin compact wideband metamaterial absorber. Radioengineering 27:364–372. ISSN 12102512. https://doi.org/10.13164/re.2018.0364

22. Nguyen TT, Lim S (2018) Design of metamaterial absorber using eight-resistive-arm cell for simultaneous broadband and wide-incidence-angle absorption. Sci Rep 8(1):6633

23. Verma A, Meena OP (2023) Design and analysis of a compact ultrathin penta-band metamaterial absorber. Sādhanā 48(4):285

24. Sharma A, Panwar R, Khanna R (2019) Experimental validation of a frequency-selective surface-loaded hybrid metamaterial absorber with wide bandwidth. IEEE Magn Lett 10:1–5

25. Mishra RK, Gupta RD, Datar S (2021) Metamaterial microwave absorber (MMA) for electromagnetic interference (EMI) shielding in X-band. Plasmonics 16(6):2061–2071

26. Sood D, Tripathi CC (2015) A wideband ultrathin low profile metamaterial microwave absorber. Microw Opt Technol Lett 57(12):2723–2728

27. Rani N, Bohre AK, Bhattacharya A (2023) An ultra-thin substrate-based conformal meta-absorber for EMI shielding and RCS minimization in c and x band. Plasmonics, pages 1–10

28. Beeharry T, Yahiaoui R, Selemani K, Ouslimani HH (2018) A dual layer broadband radar absorber to minimize electromagnetic interference in radomes. Sci Rep 8(1):382

29. Jahan MSTI, Faruque MRI, Hossain MB, Abdullah S (2023) An ultra-thin, triple-band, incident angle-insensitive perfect metamaterial absorber. Materials 16(4):1623

30. Ramya S, Rao IS (2017) A compact ultra-thin ultra-wideband microwave metamaterial absorber. Microw Opt Technol Lett 59(8):1837–1845

31. de Araújo JBO, Siqueira GL, Kemptner E, Weber M, Junqueira C, Mosso MM (2020) An ultrathin and ultrawideband metamaterial absorber and an equivalent-circuit parameter retrieval method. IEEE Trans Antennas Propag 68(5):3739–3746

32. Ghosh S, Srivastava KV (2014) An equivalent circuit model of FSS-based metamaterial absorber using coupled line theory. IEEE Antennas Wirel Propag Lett 14:511–514

33. Smith DR, Padilla WJ, Vier DC, Nemat-Nasser SC, Schultz S (2000) Composite medium with simultaneously negative permeability and permittivity. Phys Rev Lett 84(18):4184

34. Yuan X, Zhang C, Chen M, Cheng Q, Cheng X, Huang Y, Fang D (2018) Wideband high-absorption electromagnetic absorber with chaos patterned surface. IEEE Antennas Wirel Propag Lett 18(1):197–201

35. Sood D, Tripathi CC (2017) A compact ultrathin ultra-wideband metamaterial microwave absorber. J Microw Optoelectron Electromagn Appl 16:514–528

36. Zhou D, Huang X, Du Z (2016) Analysis and design of multi-layered broadband radar absorbing metamaterial using the 3-D printing technology-based method. IEEE Antennas Wirel Propag Lett 16:133–136